RSC Advances

PAPER

View Article Online
View Journal | View Issue

Cite this: *RSC Adv.*, 2025, **15**, 27113

Insight into the effect of Mg-substitution on the electronic, optoelectronic, and hydrogen storage density of NbH_2 fluorite structured: a DFT study†

Godwin O. Igomah,[a] Favour A. Nelson, *[b] Fadhil Faez Sead,[c] Musa Runde,[de] Ismail Hossain[f] and Ayi A. Ayi [b]

In the quest for multifunctional hydrogen storage materials, this study investigates the structural, electronic, and optical properties of NbH_2, MgH_2, and a series of Mg-substituted NbH_2 compounds (Mg-NbH_2, Mg_2-NbH_2, and Mg_3-NbH_2) using first-principles density functional theory (DFT) based on GGA/PBE and HSE03 methods. The motivation stems from the need to overcome the well-known limitations of MgH_2, particularly its high desorption temperature and poor reversibility, by introducing Mg into the NbH_2 fluorite framework. Structural optimization revealed a fluorite-type geometry, with Mg substitution inducing moderate lattice distortion and increasing unit cell volume from 97.22 to 103.45 Å^3. The Mg-NbH_2 system achieved a high density of 10.78 g cm^{-3} and exhibited a favorable hydrogen gravimetric capacity of 3.33 wt%, offering a promising trade-off between storage potential and structural stability. Electronic structure analysis confirmed metallicity across all substituted systems, while MgH_2 retained a non-metallic nature. A progressive decrease in total density of states was observed from 7.0 (NbH_2) to 2.0 (Mg_3-NbH_2), suggesting tunable electronic characteristics. Optical studies revealed that Mg-NbH_2 displayed the strongest dielectric response ($\varepsilon_2 \approx 85$), the highest refractive index ($n_1 \approx 3.2$), and reduced optical losses compared to its parent compounds. Notably, it retained a high optical conductivity (~13 S m^{-1}) and strong absorption in the visible range, making it a potential candidate for photocatalytic and optoelectronic applications. These results demonstrate that Mg substitution into NbH_2 significantly enhances its multifunctional behavior, offering a viable pathway to improve hydride-based materials for advanced hydrogen storage and light-harvesting technologies.

Received 4th June 2025
Accepted 14th July 2025

DOI: 10.1039/d5ra03949e

rsc.li/rsc-advances

1. Introduction

Hydrogen energy is a cornerstone of clean energy technologies due to its high energy density, abundance, and eco-friendly nature. Metal hydrides have gained significant attention from various hydrogen storage materials due to their reversible hydrogen absorption and desorption capabilities.[1] Transition metal hydrides, particularly those based on niobium (Nb), exhibit favorable thermodynamic and kinetic properties for hydrogen storage.[2] Niobium dihydride (NbH_2) with a fluorite crystal structure represents a promising candidate because it stores considerable amounts of hydrogen while maintaining structural integrity.[3] However, one of the prevailing challenges in advancing hydrogen storage systems lies in optimizing their storage density, electronic conductivity, and optical characteristics, which influence material performance in real-world applications. In this regard, substitutional doping, especially with lightweight and electropositive elements such as magnesium (Mg), has been widely explored as a strategic approach to tailor the intrinsic properties of metal hydrides. Mg-substitution has the potential to enhance the hydrogen storage capacity, tune the electronic band structure, and improve optoelectronic performance through lattice modification and charge redistribution.[4,5]

Magnesium (Mg), an alkaline earth metal with atomic number 12, is known for its low atomic weight, high electropositivity, and abundance in the Earth's crust. Its favorable characteristics, including a small ionic radius (0.72 Å) and good thermal and chemical stability, make it an attractive candidate for substitutional doping in various materials.[6,7] The ability of Mg^{2+} ions to replace other cations in crystal lattices enables the

[a]*Department of Physics, Faculty of Physical Sciences, University of Calabar, Calabar, Nigeria*
[b]*Department of Pure and Industrial Chemistry, University of Calabar, Calabar, Nigeria. E-mail: azogorfavour@gmail.com*
[c]*Department of Dentistry, College of Dentistry, The Islamic University, Najaf, Iraq*
[d]*Department of Research Analytics, Saveetha Dental College and Hospitals, Saveetha Institute of Medical and Technical Sciences, Saveetha University, Chennai, India*
[e]*National Open University of Nigeria (NOUN), Abuja, Nigeria*
[f]*Department of Nuclear and Renewable Energy, Ural Federal University, Yekaterinburg, 620002, Russia*

† Electronic supplementary information (ESI) available. CCDC 2469703–2469707. For ESI and crystallographic data in CIF or other electronic format see DOI: https://doi.org/10.1039/d5ra03949e

tuning of electronic, structural, optical, and chemical properties of host compounds.[8] In materials research, Mg-substitution has been explored extensively across ceramics, hydrides, semiconductors, and biomaterials due to its role in enhancing functionality and performance.[9,10] The influence of Mg-substitution has been well-documented in calcium phosphate-based ceramics. A study on Mg-substituted tricalcium phosphate (TCP) demonstrated that partial replacement of Ca^{2+} ions with Mg^{2+} leads to measurable structural changes.[11] Specifically, the substitution resulted in a contraction of the unit cell, as indicated by shifts in X-ray diffraction (XRD) peaks and a linear decrease in unit cell parameters (a_0 and c_0) and molar volume (V_0) with increasing Mg content (up to 10 mol%). These structural modifications suggest that Mg^{2+} ions are readily incorporated into the TCP lattice. Additionally, the substitution significantly reduced the dissolution rate of the resulting material in aqueous solution, indicating improved chemical stability, a desirable feature for biomedical applications. Hydroxyapatite ($Ca_{10}(PO_4)_6(OH)_2$), the principal mineral component of human bone and teeth, has also been the subject of extensive Mg-substitution studies.[12] High-precision hybrid DFT calculations and experimental synthesis revealed that Mg incorporation into HAP causes a reduction in lattice parameters and a noticeable distortion in the structure.[13] The substitution at different calcium sites (Ca_1 and Ca_2) alters the electronic structure, energy levels, band gap, and bulk modulus. Particularly, substitution at the Ca_2 site was more thermodynamically favorable and had a stronger effect on the infrared (IR) spectra and local structural asymmetry. These changes in local bonding environments directly influence the optical and electronic properties of HAP, making Mg-substituted HAP suitable for controlled reactivity in biological and photocatalytic systems. Interestingly, while low Mg content had a limited impact on basic catalytic reactivity, higher Mg concentrations led to structural disorder and nonstoichiometry, reducing the number of active basic sites. In such cases, new phases such as whitlockite were observed, highlighting a concentration-dependent tradeoff between structural stability and functionality. This aligns with the broader understanding that substitution levels must be carefully optimized to avoid undesired phase transitions or defect formation.

The motivation for this study stems from the growing need to enhance the hydrogen storage capacity and optoelectronic performance of existing fluorite-type metal hydrides. Among them, NbH_2 stands out due to its stable fluorite structure, favorable electronic conductivity, and intrinsic hydrogen affinity.[14,15] However, its hydrogen storage density and band gap characteristics remain suboptimal for advanced applications. Magnesium (Mg) was chosen as a dopant owing to its light atomic weight, high hydrogen gravimetric capacity, and known ability to enhance sorption kinetics when alloyed with transition metals. Unlike heavier dopants, Mg offers the dual benefit of reducing system weight while potentially modifying the band structure and boosting hydrogen density.[16] Thus, this study aims to explore how Mg-substitution affects the structural stability, electronic properties, and hydrogen storage potential of NbH_2. The novelty of the work lies in its systematic application of density functional theory (DFT) to uncover the atomistic effects of Mg incorporation in NbH_2, a relatively unexplored yet promising material for multifunctional energy applications.

2. Computational methods

First-principles calculations based on density functional theory (DFT) were performed using the CASTEP module implemented in Materials Studio 2020.[17] The calculations in this study were performed using density functional theory (DFT) within the generalized gradient approximation (GGA), employing the Perdew–Burke–Ernzerhof (PBE) functional to describe the exchange–correlation interactions.[18] Relativistic effects were treated using the Koelling–Harmon scalar relativistic approximation.[19] The electronic wavefunctions were expanded in a plane-wave basis set with a cutoff energy of 381 eV. Electronic convergence was achieved with an energy tolerance of 2×10^{-6} eV per atom and an eigenvalue convergence criterion of 8.889×10^{-7} eV. The charge density was mixed using the Pulay scheme,[20] with a maximum mixing history length of 20, a mixing amplitude of 0.5, and a *g*-vector cut-off of 1.5 $Å^{-1}$. Geometry optimization was carried out using the Broyden–Fletcher–Goldfarb–Shanno (BFGS) algorithm under fixed basis quality conditions.[21] The maximum number of ionic steps was set to 100, with convergence criteria for the total energy, maximum ionic force, and atomic displacement set at 2×10^{-5} eV per atom, 0.05 eV $Å^{-1}$, and 0.002 Å, respectively. To improve the accuracy of the calculated band structures and structural parameters (lattice constants), the Heyd–Scuseria–Ernzerhof (HSE03) hybrid functional was employed as a post-processing correction.[22] The HSE03 functional provides a more reliable description of the electronic structure by incorporating a portion of exact Hartree–Fock exchange, which is particularly important for systems where bandgap and structural precision are critical.

3. Results and discussion

3.1 Bonding characteristics, population analysis, and hybridization

To understand the effect of Mg substitution on the bonding nature within the NbH_2 fluorite structure, a detailed population and bond length analysis was performed using the Mulliken scheme. The goal was to quantify the bonding strength between H, Nb, and Mg atoms, as well as to assess how increasing Mg content influences electron distribution and interatomic interactions within the lattice. In pristine NbH_2, the H–Nb bond length is 1.978 Å with a bond population of 0.35, indicating a moderately covalent character. The H–H interaction shows a negative bond population of −0.07, suggesting weak repulsive or nonbonding interactions between hydrogen atoms within the lattice.[23,24] Upon Mg doping, significant changes in bonding patterns are observed. For instance, in the Mg-NbH_2 compound, while the H–Nb bond population drops sharply to 0.06 (nearly nonbonding), new H–Mg interactions form with a bond population of 0.17, indicating weak ionic bonding. As Mg content

increases in Mg_2-NbH_2 and Mg_3-NbH_2, the H–Nb bond population remains low (0.12 and 0.03 respectively), while the H–Mg bond population increases to 0.29 and then decreases to 0.15. These trends imply that Mg substitution progressively disrupts the original Nb–H bonding network and introduces ionic H–Mg interactions, which may facilitate hydrogen release due to weaker bonding. A comparative analysis with pure MgH_2 supports this observation. The H–Mg bond population in MgH_2 is as high as 0.57, indicating a significantly stronger ionic character compared to Mg-NbH_2 variants. Moreover, the H–H population in MgH_2 is highly negative (−0.68), suggesting stronger hydrogen–hydrogen repulsion, which may relate to higher desorption kinetics.

The atomic Mulliken population data (Table S2†) further reinforce these conclusions. In pristine NbH_2, the Nb atom exhibits a total electronic population of 15, with notable contributions from the d-orbital (4.084), reflecting its role in covalent bonding. As Mg atoms are introduced, the overall electronic populations increase with higher s- and p-orbital character (*e.g.*, Mg-NbH_2 shows a total of 56.997 electrons), suggesting a shift toward more ionic behavior. Particularly in Mg_2-NbH_2 and Mg_3-NbH_2, the electron populations become more delocalized, and d-orbital participation drops significantly (to ∼4.1), indicating weakened Nb-based bonding. In pure MgH_2, the electron population is predominantly from s- and p-orbitals (5.217 and 6.783, respectively), aligning with its known ionic bonding nature.[25,26]

In summary, these bonding analyses reveal that Mg substitution in NbH_2 reduces the covalent character of the Nb–H bonds and introduces weaker, more ionic Mg–H interactions. This change in bonding environment weakens the hydrogen binding energy, potentially improving desorption properties. Additionally, the disruption of the Nb–H network by Mg alters the electron distribution within the lattice, which may also influence the material's optoelectronic and catalytic behavior.

3.2 Structural analysis

NbH_2 and MgH_2 both adopt a fluorite-type structure within the cubic $Fm\bar{3}m$ space group. In NbH_2, Nb^{2+} ions exhibit a face-centered cubic coordination with eight H^{1-} atoms, featuring Nb–H distances of 1.98 Å. Each hydride ion connects to four Nb^{2+} centers, forming mixed corner- and edge-sharing HNb_4 tetrahedra. Similarly, in MgH_2, Mg^{2+} ions are surrounded by eight H^{1-} atoms in a comparable geometry, with bond lengths of 2.06 Å. Here, each H^{1-} ion coordinates with four Mg^{2+} atoms, resulting in HMg_4 tetrahedral units that also share corners and edges.[27] The structural analysis of NbH_2, MgH_2, and their magnesium-substituted derivatives reveals significant differences depending on the exchange–correlation functional used in the DFT calculations, namely, PBE and HSE03. Under the PBE functional, NbH_2 displays a distorted orthorhombic symmetry with lattice constants $a = c = 4.65$ Å and $b = 4.47$ Å, resulting in a unit volume of 96.65 Å^3 and a density of 6.52 g cm^{-3}. This closely aligns with the 4.57 Å lattice constant reported by Xiaobing *et al.* for NbH_2.[27] MgH_2, on the other hand, exhibits a larger unit cell volume (112.60 Å^3) with lattice constants around 4.81–4.86 Å and a much lower density of 1.55 g cm^{-3}, which slightly exceeds the 4.77 Å reported by Vajeeston *et al.*[28] A known characteristic of the PBE functional is its tendency to slightly overestimate lattice dimensions. With increasing Mg content in the Mg_{1-3}-NbH_2 series, there is a gradual increase in unit volume (from 97.22 to 103.45 Å^3) and density (up to 10.78 g cm^{-3}), accompanied by angular distortions in Mg-NbH_2 ($\alpha = 94°$, $\beta = 92°$, $\gamma = 88°$), indicating a loss of perfect cubic symmetry and increasing structural distortion due to doping.

In contrast, the HSE03 functional maintains a constant unit volume (95.39 Å^3) and lattice parameter (4.57 Å) across all compounds, regardless of composition. While this value aligns well with the experimental lattice constant for NbH_2 reported by Xiaobing *et al.*, the uniformity in volume and geometry across all doped systems, including MgH_2, appears unrealistic. This suggests that the structures under HSE03 may not have undergone full relaxation or were constrained during optimization, making the results less physically meaningful for structural evaluation. Correspondingly, the densities calculated under HSE03 decrease with increasing Mg content, from 6.61 g cm^{-3} (NbH_2) to 3.03 g cm^{-3} (Mg_3-NbH_2), which contradicts the expected trend of increasing mass and decreasing volume.

The enthalpy and total energy parameters derived from both PBE and HSE03 functionals provide essential insights into the thermodynamic stability of NbH_2 and its Mg-substituted derivatives. Under the PBE functional, the total energy of NbH_2 is −6.75 eV, with a corresponding enthalpy of −6.75 eV. As Mg is gradually introduced into the NbH_2 framework to form Mg-NbH_2, Mg_2-NbH_2, and Mg_3-NbH_2, the total energy becomes increasingly negative (−6788.06 eV, −6822.37 eV, and −6855.15 eV, respectively), indicating the growing size and atomic complexity of the systems. Although total energy values are not directly comparable across compounds of different compositions, the enthalpy values, which range from −6.79 eV to −6.86 eV across these substituted structures, suggest a trend toward improved thermodynamic stability with increasing Mg content. MgH_2 exhibits the most negative enthalpy value at −6.89 eV, suggesting it is the most stable compound among those studied. A similar trend is observed under the HSE03 functional. The total energy of NbH_2 is −699.49 eV with an enthalpy of −0.70 eV. As Mg substitution increases, the total energies of Mg-NbH_2, Mg_2-NbH_2, and Mg_3-NbH_2 decline significantly to −2139.97 eV, −3582.32 eV, and −5022.71 eV, respectively, while their enthalpy values follow a corresponding downward trend from −2.14 eV to −5.02 eV. MgH_2 again shows the most negative enthalpy at −6.46 eV, confirming its superior thermodynamic stability. While both functionals support the conclusion that Mg incorporation enhances the stability of NbH_2-based compounds, PBE tends to yield slightly more negative enthalpy values, possibly due to its tendency to overbind. In contrast, HSE03, a hybrid functional, provides more moderate estimates but still reinforces the general stability trend. The consistent decrease in enthalpy with increasing Mg content across both computational methods underscores the

Table 1 Calculated structural, energetic, and vibrational properties of NbH_2, MgH_2, and Mg-substituted NbH_2 compounds (Mg-NbH_2, Mg_2-NbH_2, Mg_3-NbH_2) using the GGA–PBE functional. Reported parameters include unit cell volume, density, lattice constants (*a*, *b*, *c*), total energy, enthalpy of formation, bulk modulus, and the highest vibrational mode (Γ-point frequency in cm^{-1})

Compounds	Unit volume (A^3)	Unit density (g cm^{-3})	Lattice constants			Total energy (eV)	Enthalpy (eV)	Bulk modulus (GPa)	Frequency (cm^{-1})
			a	*b*	*c*				
NbH_2	96.65	6.52	4.65	4.47	4.65	−6754.24	−6.75	318.63	1668
Mg-NbH_2	97.22	8.15	4.71	4.56	4.55	−6788.06	−6.79	209.42	1668
Mg_2-NbH_2	98.11	9.72	4.52	4.81	4.52	−6822.37	−6.82	156.96	1321.48
Mg_3-NbH_2	103.45	10.78	4.67	4.76	4.65	−6855.15	−6.86	6.27	6151.39
MgH_2	112.60	1.55	4.86	4.81	4.81	−6888.58	−6.89	869.24	1668

favorable energetic landscape of Mg-doped NbH_2 hydrides, with MgH_2 emerging as the most stable configuration.

From a mechanical standpoint, the PBE functional shows a progressive decrease in bulk modulus from 318.63 GPa (NbH_2) to just 6.27 GPa (Mg_3-NbH_2), indicating significant softening and structural weakening upon doping. Notably, MgH_2 exhibits an unusually high bulk modulus (869.24 GPa), possibly due to tighter packing or bonding interactions. HSE03 did not report bulk modulus values, limiting direct mechanical comparison. Vibrational frequency trends further support the reliability of PBE for structural behavior, showing consistent values for undoped compounds (1668 cm^{-1}), while HSE03 reveals a progressive increase in frequency with doping from 1163.69 cm^{-1} in Mg-NbH_2 to 3836.40 cm^{-1} in Mg_3-NbH_2 though the unusually high values, especially in PBE for Mg_3-NbH_2 (6151.39 cm^{-1}), suggest computational anomalies or strong local modes. The vibrational frequencies listed in Tables 1 and 2 represent the maximum optical phonon mode at the Γ-point, derived from lattice dynamics calculations. These frequencies provide insight into the vibrational behavior of the H atoms in the lattice, which is critical for evaluating hydrogen bonding strength, lattice dynamics, and the potential for reversible hydrogen desorption.[29] Higher frequencies are typically associated with strong metal–H interactions and dynamic stability, while lower frequencies may reflect weakened bonding or soft modes due to structural distortion or increased Mg substitution.

The differences between the GGA–PBE values (Table 1) and those obtained using HSE03 (Table 2) arise from the known limitations of the GGA functional, which tends to underestimate bandgaps and yields functional-dependent absolute energies. Nonetheless, GGA–PBE is suitable for assessing structural trends, relative stabilities, and vibrational characteristics across chemically similar compounds, and all values within each table are internally consistent. In summary, the PBE functional more accurately captures the structural evolution and distortion due to Mg substitution in NbH_2, reflecting realistic trends in lattice parameters, unit cell volume, density, and mechanical stability. Meanwhile, HSE03, although aligning precisely with some literature values for NbH_2, offers limited structural flexibility and possibly constrained optimization, making it less suitable for analyzing doping-induced changes. Therefore, for structural analysis involving substitutional effects, PBE appears to provide more reliable and physically consistent results (Fig. 1).

3.3 Electronic analysis: band structure and PDOS

The electronic properties of the studied compounds were investigated through both GGA–PBE and HSE03 functionals, providing insights into their band structure and density of states (DOS) characteristics. The GGA–PBE band structure in Fig. 2 reveals that the compounds exhibit conducting behavior, with the conduction band minimum (CBM) and valence band maximum (VBM) overlapping one another. This is except for MgH_2, whose CBM and VBM are located at different *k*-points (indicating an indirect band gap) or at the same *k*-point (for direct band gap systems). However, the band gaps obtained from GGA–PBE are generally underestimated, a known limitation of this functional.[18] This shortcoming is addressed in the HSE03 band structure plots in Fig. 3. The HSE03 functional shows precisely the same results as those from GGA–PBE, which

Table 2 Structural, energetic, and vibrational properties of the studied hydrides computed using the HSE03 hybrid functional. This includes unit cell volume, density, lattice constants, total energy, enthalpy of formation, and maximum vibrational frequency (in cm^{-1}). The data are used to validate and complement the GGA–PBE results

Compounds	Unit volume (A^3)	Unit density (g cm^{-3})	Lattice constants	Total energy (eV)	Enthalpy (eV)	Bulk modulus (GPa)	Frequency (cm^{-1})
			$a = b = c$				
NbH_2	95.39	6.61	4.57	−699.49	−0.70	—	1668
Mg-NbH_2	95.39	5.24	4.57	−2139.97	−2.14	—	1163.69
Mg_2-NbH_2	95.39	4.22	4.57	−3582.32	−3.58	—	1255.92
Mg_3-NbH_2	95.39	3.03	4.57	−5022.71	−5.02	—	3836.40
MgH_2	95.39	1.83	4.57	−6463.42	−6.46	—	1668

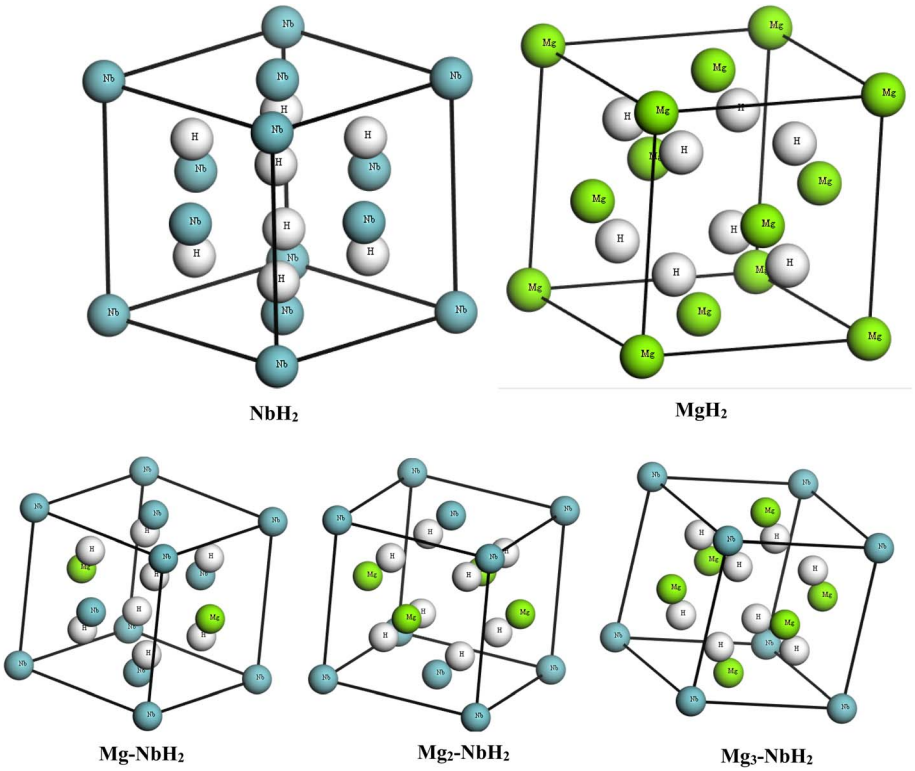

Fig. 1 Optimized crystal structures of NbH_2, MgH_2, and Mg-substituted NbH_2 (Mg-NbH_2, Mg_2-NbH_2, Mg_3-NbH_2) showing their fluorite-derived configurations. Atoms are color-coded by element to emphasize structural distortion due to Mg substitution.

confirms that the GGA–PBE method used is accurate. Conducting materials like Mg-NbH_2, which exhibit metallic behavior due to the presence of electronic states at the Fermi level, are valuable in a wide range of technological applications that require efficient charge transport. The use of such materials is in electrical contacts and interconnects within electronic devices, where their low resistivity ensures minimal energy loss and high current-carrying capacity.[30] In addition, conducting hydride-based compounds have potential in hydrogen storage and sensing applications, where their electrical conductivity can facilitate real-time monitoring of hydrogen uptake or release *via* resistive or impedance-based methods.[31] Generally, the metallic nature of these compounds makes them suitable for integration into next-generation energy devices, sensors, and electronic systems where conductivity and functional reactivity are both required.

The PDOS and TDOS plots in Fig. 3 offer a more detailed understanding of the electronic structure by showcasing the contribution of specific atomic orbitals to the electronic states near the Fermi level.[32] In the PDOS, the valence band is predominantly composed of s-orbital contributions from the smaller atoms (such as Mg and H, depending on the composition), while the conduction band shows significant contributions from the d-orbitals of the metal center of Nb. All the compounds show three peaks, except MgH_2, which is fully occupied by the s-orbitals in bonding. NbH_2 shows a TDOS of 7, a d-orbital contribution of 3.5, and an s-orbital contribution of 4. MgH_2 shows a TDOS contribution of 3.5 and an s-orbital contribution of 2.8. Mg-NbH_2 shows a TDOS of 5.8, d-orbital contribution of 3, and s-orbital contribution of 3.2. Mg_2-NbH_2 shows a TDOS contribution of 5, a d-orbital contribution of 2.9, and an s-orbital contribution of 3. Mg_3-NbH_2 shows a TDOS contribution of 2, a d-orbital contribution of 3.8 and 3.3. From this, it is observed that the substitution of Mg in NbH_2 reduces the TDOS contribution as well as the d-orbital contribution and but increases the s-orbital contribution as compared to the parent compound NbH_2. This indicates strong hybridization between the metal d-states and the non-metal s-states, suggesting covalent bonding interactions that could influence charge mobility.[33] The TDOS further supports these observations by displaying the overall electronic density distribution, with pronounced peaks near the valence and conduction band edges, implying localized states that are important for optical transitions. In summary, the combination of band structure and DOS analyses illustrates that the compounds are conductors with substantial orbital hybridization. The discrepancy between the PBE and HSE03 results underlines the importance of using hybrid functionals for accurate electronic property predictions (Fig. 4).

3.4 Optoelectronic analysis

3.4.1 Optical absorption, reflectivity, and loss function. The optoelectronic properties of the studied compounds NbH_2, Mg-NbH_2, Mg_2-NbH_2, Mg_3-NbH_2, and MgH_2 were evaluated based on their absorption coefficient, reflectivity, and energy loss function across the photon energy range of 0 to 80 eV, as

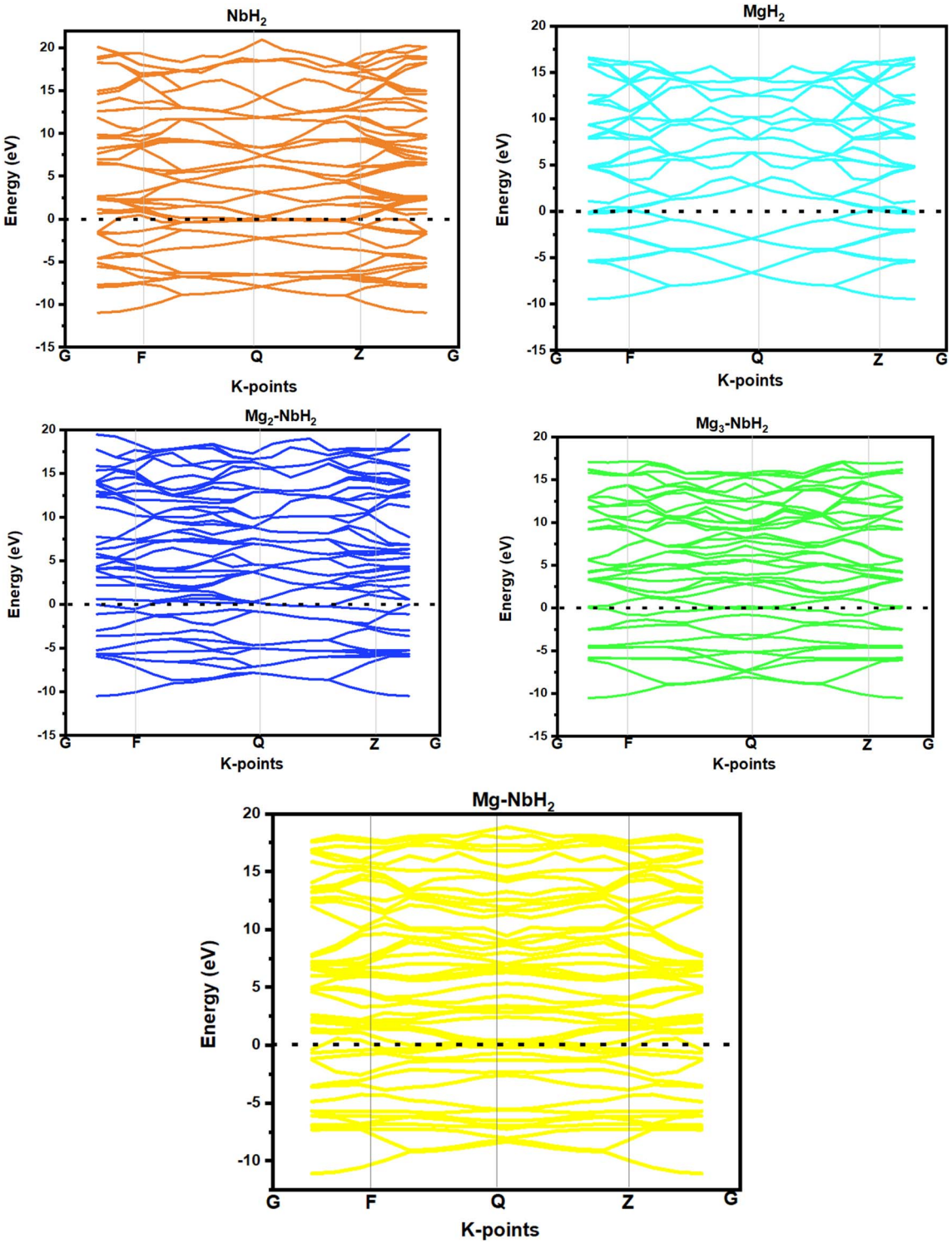

Fig. 2 Electronic band structures of NbH_2, MgH_2, and Mg-substituted NbH_2 compounds calculated using the GGA–PBE functional. The band dispersion is plotted along high-symmetry directions of the $Fm\bar{3}m$ Brillouin zone. The Fermi level is aligned to 0 eV.

shown in the provided plots. In the absorption plot, NbH_2 exhibits the highest absorption coefficient across the spectrum, peaking around 5.5×10^5 in the energy range of approximately 30–40 eV, indicating its superior capability for absorbing high-energy photons. This suggests potential for optoelectronic applications where strong photon–material interaction is required.[34] The incorporation of magnesium into NbH_2 generally reduces the absorption strength, with Mg_2-NbH_2 and Mg_3-NbH_2 showing the lowest absorption intensities, suggesting that increased Mg content diminishes the optical absorption

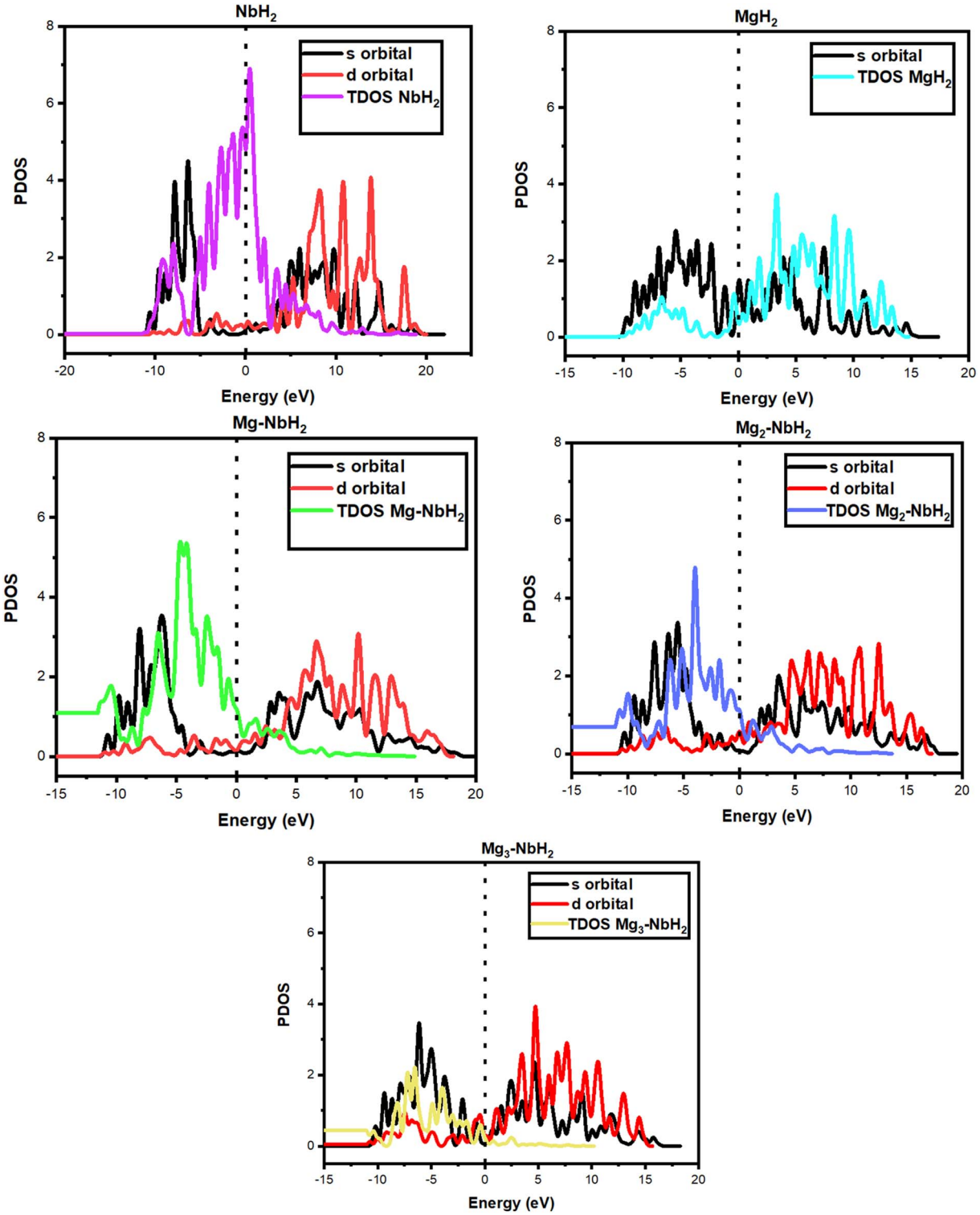

Fig. 3 Total and partial density of states (TDOS and PDOS) for the studied compounds obtained with the GGA–PBE method. The contribution of individual atomic orbitals (Nb d, Mg s, H s) is highlighted to reveal electronic characteristics and bonding behavior.

performance. MgH_2, although a separate phase, shows moderate absorption primarily in the lower energy range (5–25 eV), reflecting different electronic transitions compared to the Nb-containing compounds.

Reflectivity analysis discloses that MgH_2 demonstrates an exceptionally high reflectivity (approaching 1.0) in the low-energy region (below 10 eV), significantly higher than all other compounds. This implies strong surface reflection of incident

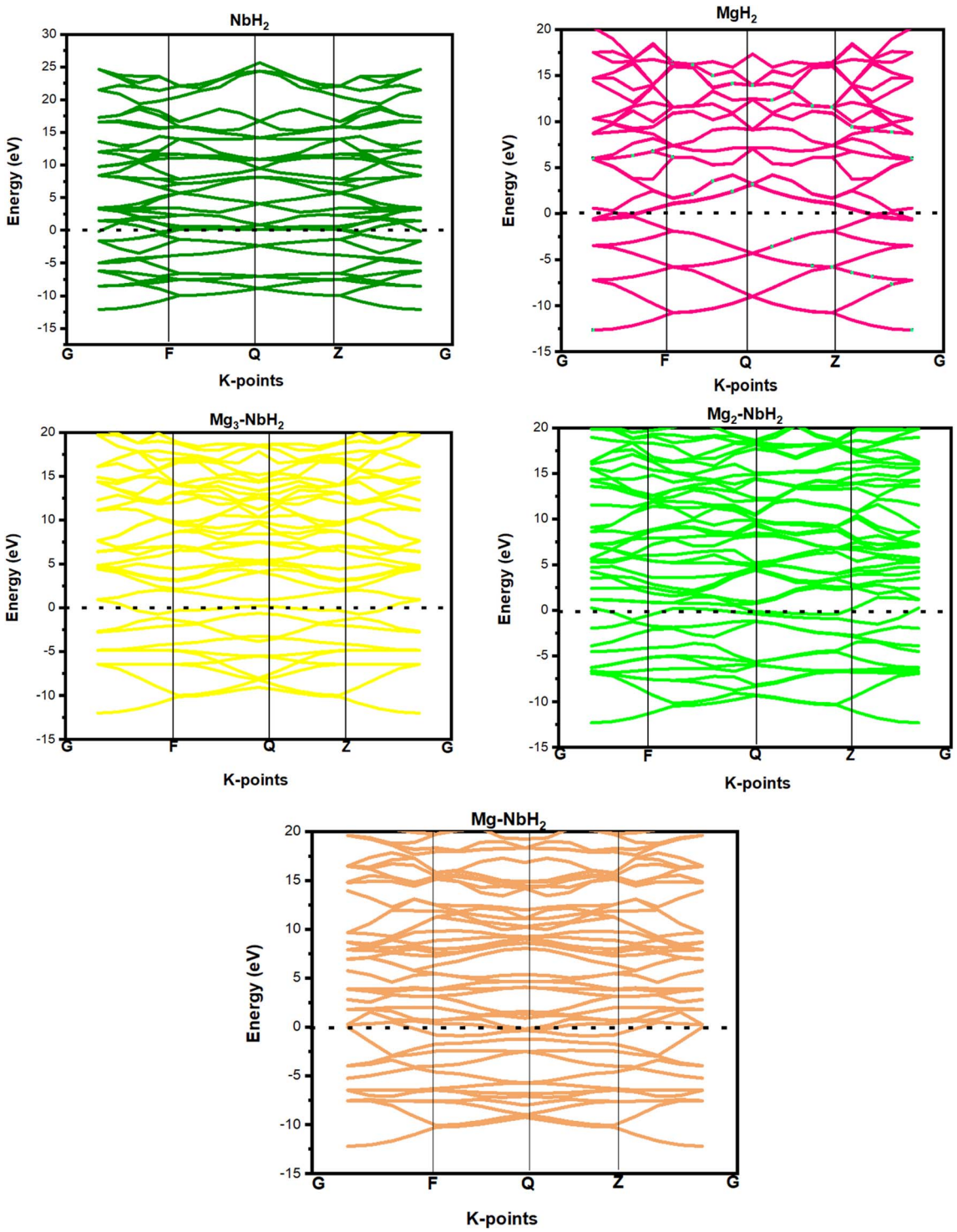

Fig. 4 Electronic band structures of NbH_2 and Mg-substituted NbH_2 calculated using the HSE03 functional, along high-symmetry directions of the $Fm\bar{3}m$ Brillouin zone. The Fermi level is set to 0 eV. These results are used to cross-validate GGA–PBE predictions.

light, which may reduce its suitability for applications requiring light penetration.[35] NbH_2 shows moderate reflectivity throughout the spectrum, while the Mg-doped variants, especially Mg_2-NbH_2 and Mg_3-NbH_2, show reduced reflectivity, indicating improved photon absorption capabilities in those regions.

The loss function plot, which provides understanding on the energy loss of fast electrons traversing the material,[36] is particularly dominated by a sharp peak for MgH_2 around 10 eV, reaching a maximum value of 60. This signifies a strong plasmon resonance in MgH_2, indicative of collective oscillations of the electron gas. In contrast, the other compounds exhibit lower

and broader peaks, suggesting less intense plasmonic activity. NbH_2 and its Mg-doped variants show moderate loss function values in the 10–30 eV range, with multiple smaller peaks, pointing to more complex electronic transitions and weaker plasmonic behavior. Inclusively, NbH_2 stands out for its high absorption and moderate reflectivity, making it a promising candidate for energy harvesting or UV shielding applications. The Mg incorporation tunes the optical response, potentially allowing for the engineering of materials with tailored optoelectronic characteristics. MgH_2, with its intense reflectivity and sharp energy loss peak, is more reflective and plasmonically active, which may be beneficial in applications involving light reflection or plasmonic enhancement (Fig. 5).

3.4.2 Optical conductivity. Optical conductivity refers to a material's response to an electromagnetic field (light) in terms of its ability to conduct electricity at various frequencies, especially in the visible and near-visible spectrum. It is a frequency-dependent counterpart of electrical conductivity denoted as $\sigma(\omega)$, where σ is the conductivity and ω is the angular frequency of the light.[37] This physical property is described by the real part of the optical conductivity ($Re[\sigma(\omega)]$) which involves energy dissipation (*i.e.*, absorption of light) and the imaginary part of the optical conductivity ($[Im\ \sigma(\omega)]$) which is related to energy storage in the medium.[38] In Fig. 6, the plots for the real and imaginary optical conductivities are shown for the studied compounds. Starting with the real conductivity plot, MgH_2 (blue) shows the highest peak at 13 s m^{-1} followed by NbH_2 (black) at 9 s m^{-1}, Mg-NbH_2 (red) shows a peak at 8 s m^{-1}, Mg_3-NbH_2 (green) at 6.3 s m^{-1} and Mg_2-NbH_2 (purple) at 6 s m^{-1}. This means that the subsequent addition of Mg to NbH_2 gradually reduces the dissipation energy thus affecting the absorption capacity of the compounds. On the other hand, complete substitution of Nb with Mg in MgH_2 shows that MgH_2 strongly interacts with light matter to enhance optical conductivity. The second plot which contains the imaginary optical conductivity shows MgH_2 to possess the highest peak at 7 s m^{-1} followed by

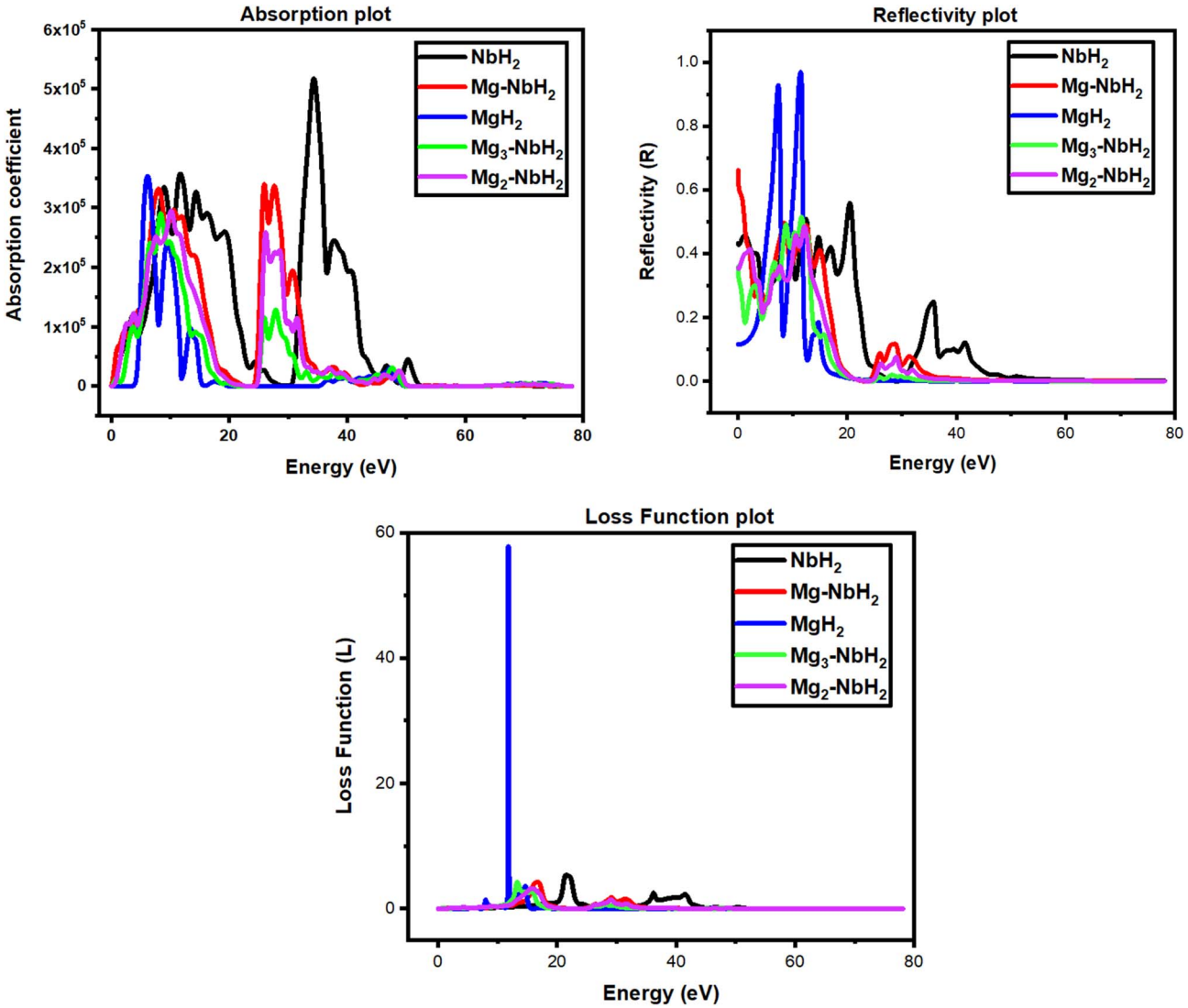

Fig. 5 Optical absorption spectra, reflectivity, and energy loss function of the studied compounds, calculated using the GGA–PBE method. The plots reveal light-harvesting potential and dielectric loss behavior relevant to photocatalysis and optoelectronics.

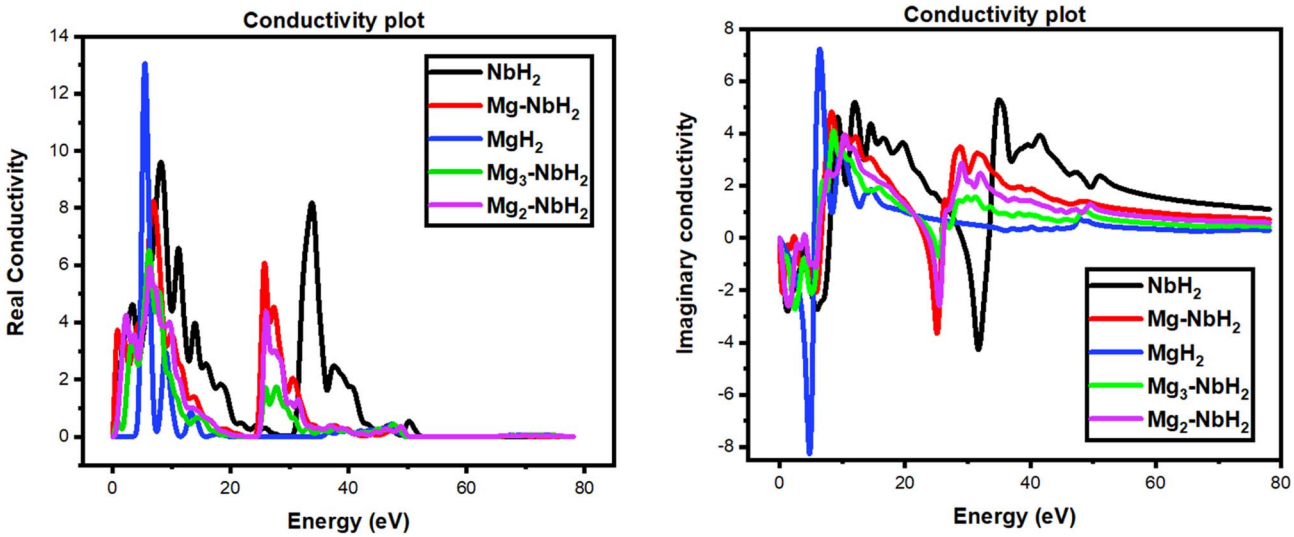

Fig. 6 Real and imaginary parts of optical conductivity for the studied compounds under GGA–PBE. These parameters indicate photon-induced charge carrier response and material conductivity in different energy regions.

NbH_2 at 5 s m^{-1}, then Mg-NbH_2 at 4.8 s m^{-1}, Mg_3-NbH_2 at 4 s m^{-1} and Mg_2-NbH_2 at 3.8 s m^{-1}. Thus, the imaginary plot follows the same route as the real plot which the concurrent reduction in conductivity as the substitution of Mg in NbH_2 increases.

3.4.3 Optical dielectric function. The dielectric function is a complex quantity that describes how a material responds to an external electric field, especially in the presence of an oscillating electromagnetic wave such as light. It is fundamental in understanding a material's optical, electronic, and energy absorption properties. Mathematically, the dielectric function is expressed as:[39]

$$\varepsilon(\omega) = \varepsilon_1(\omega) + i\varepsilon_2(\omega) \quad (1)$$

where $\varepsilon_1(\omega)$ is the real part, representing the material's ability to store electric energy (related to polarization and refractive index) while $\varepsilon_2(\omega)$ is the imaginary part, which accounts for the energy loss (*i.e.*, absorption of the electromagnetic wave by the material).[40–42]

The dielectric function plots comprising the real and imaginary parts reveal vital information on the optical response and electronic polarizability of the investigated hydride compounds.[43] Among the materials, Mg-NbH_2 demonstrates the most pronounced peaks in both the real and imaginary components of the dielectric function, indicating a strong interaction with incident electromagnetic radiation and high polarizability. Specifically, in the real part, Mg-NbH_2 peaks sharply around 0 eV with a maximum value exceeding 30, suggesting substantial static dielectric response, which aligns with its metallic behavior and delocalized charge carriers. In the imaginary part, which reflects absorption characteristics, Mg-NbH_2 again exhibits the highest peak (around 85), emphasising its strong interband transitions and enhanced optical activity.

Following Mg-NbH_2, MgH_2 shows the next highest peaks in both real and imaginary components, indicative of relatively strong optical absorption and dielectric response, consistent with its semiconducting nature. NbH_2 and Mg_3-NbH_2 exhibit moderate peaks, suggesting intermediate dielectric behavior and limited but noticeable interaction with electromagnetic fields. Lastly, Mg_2-NbH_2 shows the least pronounced peaks across both dielectric plots, implying the lowest optical absorption and static dielectric constant among the series. These trends point to Mg-NbH_2 being the most optically active and polarizable, making it a strong candidate for optoelectronic or plasmonic applications, while Mg_2-NbH_2 would be more optically inert (Fig. 7).

3.4.4 Optical refractive index. The refractive index (denoted as n) is a fundamental optical property of a material that describes how light propagates through it. It is defined as the ratio of the speed of light in a vacuum (c) to the speed of light in the material (v):[44]

$$n = \frac{c}{v} \quad (2)$$

There are two components, which include the real part (n_1) representing how much the light is bent or refracted when entering the material.[45] A higher n_1 means greater bending and stronger optical density. The imaginary part (n_2) is associated with the absorption of light within the material. A higher n indicates that the material absorbs more light and transmits less. Together, the complex refractive index is written as:[46]

$$\tilde{n}n_1 + in_2 \quad (3)$$

The refractive index plots presented illustrate both the real (n_1) and imaginary (n_2) parts of the refractive indices of the compounds NbH_2, MgH_2, Mg-NbH_2, Mg_3-NbH_2, and Mg_2-NbH_2 over a wide energy range.[47] These indices offer vital insights into the optical transparency, reflectivity, and absorption of the materials. In the real part of the refractive index (n_1) plot, Mg-

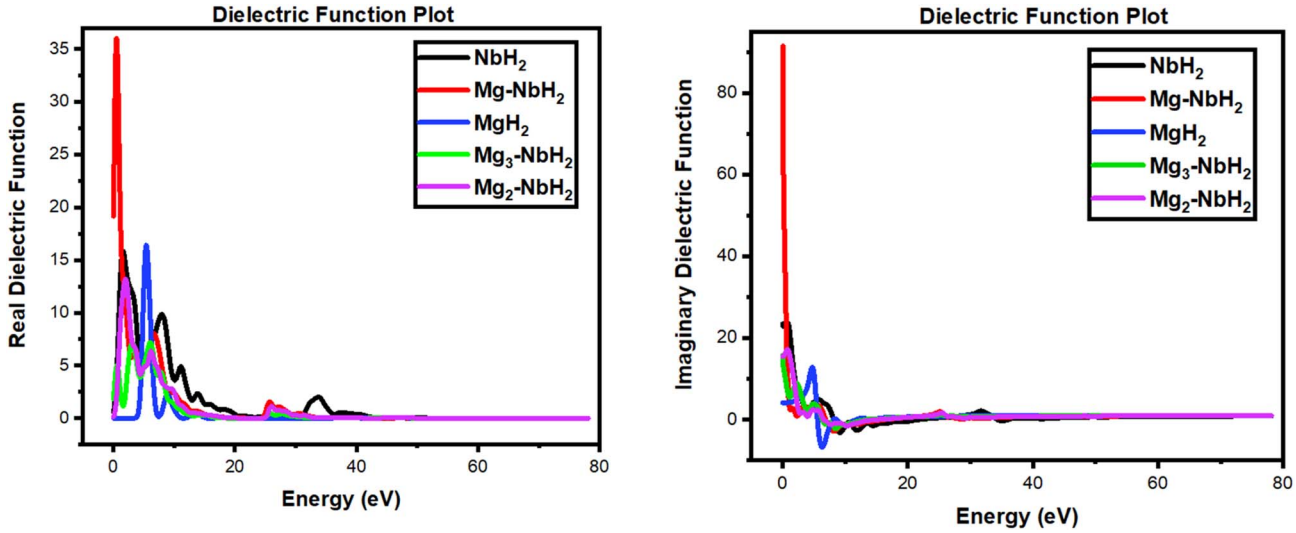

Fig. 7 Real and imaginary components of the dielectric function (ε_1 and ε_2) of the studied compounds obtained from GGA–PBE optical calculations, showing their polarizability and optical transparency across energy ranges.

NbH_2 exhibits the highest peak value of about 3.2, indicating strong light bending capability and high optical density in the low-energy region. This is followed closely by MgH_2, which also shows a significant peak above 3.0, confirming its notable dielectric response. NbH_2 presents a slightly lower peak around 2.5, while Mg_3-NbH_2 and Mg_2-NbH_2 have more moderate peaks, suggesting comparatively lower light-retardation effects. These values gradually taper off with increasing photon energy, reflecting a decrease in refractive behavior at high energies. In the imaginary part of the refractive index (n_2) plot, which relates to absorption, Mg-NbH_2 again shows the most prominent peak, exceeding 9.0, indicating it has the highest optical absorption in the visible-to-UV region. This implies greater interband transitions and energy dissipation in this material. Following this are NbH_2, MgH_2, and Mg_3-NbH_2, all exhibiting moderate absorption behaviors. Mg_2-NbH_2 has the lowest imaginary peak, suggesting it is more optically transparent and has reduced electronic losses compared to the others. These variations in the refractive indices reflect differences in the electronic structure and bonding nature of the compounds, particularly the extent of hybridization and electron delocalization. The high optical activity of Mg-NbH_2 positions it as a strong candidate for optoelectronic or photonic applications, while Mg_2-NbH_2 may be more suitable for transparent or low-loss dielectric uses (Fig. 8).

3.5 Elastic and mechanical properties

The elastic and mechanical properties of the studied compounds reveal significant insights into their structural rigidity, ductility, and stability. For all systems, the elastic constants C_{11}, C_{12}, and C_{44} play critical roles in defining their resistance to deformation. Notably, NbH_2 exhibits high stiffness with $C_{11} = 257.15$ GPa and $C_{44} = 111.15$ GPa, indicating a strong and mechanically stable structure. The Born mechanical stability criteria—$C_{11} > 0$, $C_{44} > 0$, C_{11}–$C_{12} > 0$, and $C_{11} + 2C_{12} > 0$—are satisfied by NbH_2, Mg-NbH_2, and Mg_2-NbH_2, confirming their mechanical stability.[48] However, Mg_3-NbH_2 and MgH_2 fail to meet the $C_{44} > 0$ criterion, with negative values (−8.03 and −9.27 GPa, respectively), indicating shear instability and potential mechanical failure under certain deformations.

Among the compounds, NbH_2 also possesses the highest bulk modulus (156.96 GPa), shear modulus (106.45 GPa), and Young's modulus (260.47 GPa), highlighting its superior resistance to volume change, shear deformation, and overall elastic deformation, respectively. As magnesium is incrementally added, these mechanical parameters decline, with MgH_2 having the lowest values ($B = 23.76$ GPa, $G = 20.19$ GPa, and $E = 47.21$ GPa), indicating a much softer and more ductile material. The Pugh ratio (B/G), which measures ductility, further differentiates the compounds. A value above 1.75 typically indicates ductility, while values below suggest brittleness.[49] Mg-NbH_2 has the highest B/G ratio (3.27), suggesting it is the most ductile among the set, whereas Mg_3-NbH_2 (0.97) and Mg_2-NbH_2 (1.35) lean towards brittleness. NbH_2, with a B/G of 1.47, straddles the brittle–ductile borderline. The anisotropic factor (A), which describes directional dependency of the elastic response,[50] ranges from 0.21 for NbH_2 (indicating near isotropy) to a highly negative −9.67 for Mg_3-NbH_2, suggesting severe elastic anisotropy and instability. Similarly, Poisson's ratio (υ), which reflects the degree of lateral expansion when compressed,[51] ranges anomalously, with Mg_3-NbH_2 and MgH_2 showing unrealistic values (1.59 and −10.14, respectively), further confirming their mechanical instability or computational artefacts due to soft shear modes.

In summary, the data indicate that NbH_2 is the most mechanically stable and rigid among the studied compounds. The addition of Mg modifies the mechanical behavior, with Mg-NbH_2 showing enhanced ductility but reduced stiffness, while higher Mg concentrations lead to mechanical instability, as reflected by the failure to satisfy some of the Born criteria and

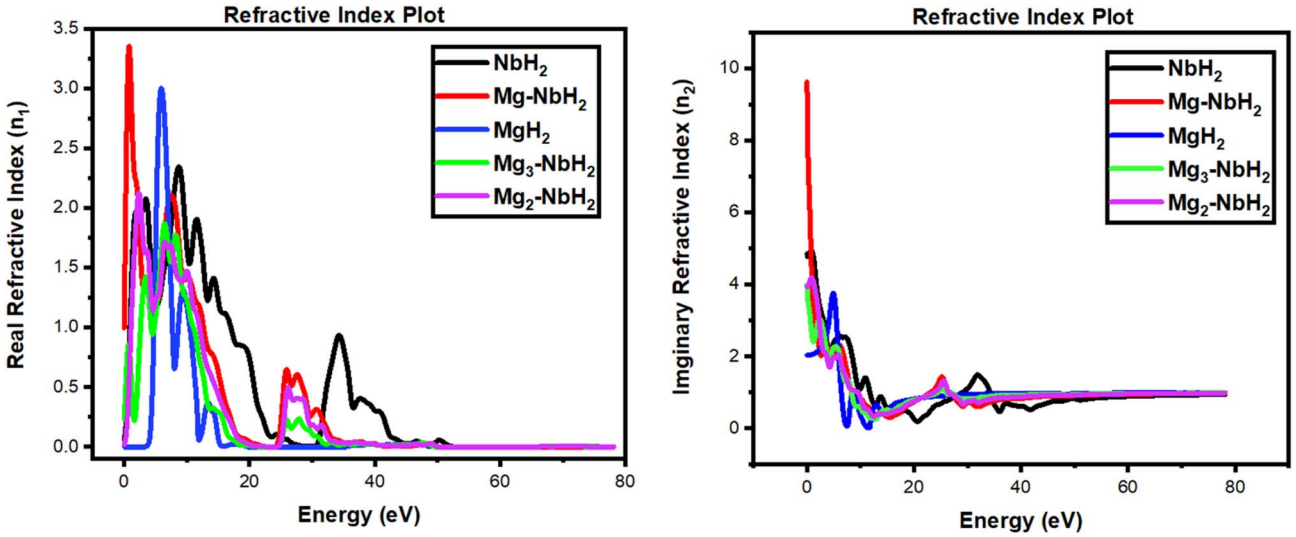

Fig. 8 Refractive index (n) and energy loss function (L) spectra (both real and imaginary parts) for the studied compounds. These optical properties provide insight into the interaction of light with the material and the onset of plasmonic behavior.

the emergence of negative or extreme values in key elastic parameters (Table 3).

3.6 Hydrogen storage capacity

The hydrogen gravimetric storage capacity of a material refers to the mass percentage of hydrogen that can be stored within the compound, which is a crucial parameter for evaluating materials for hydrogen storage applications. A higher gravimetric capacity indicates that a compound can store more hydrogen per unit mass, making it more efficient for lightweight and compact hydrogen storage systems, especially in the context of fuel cells and clean energy technologies. The formula for calculating the hydrogen gravimetric capacity is given as:[52]

$$\text{hydrogen gravimetric capacity (wt\%)} = \frac{\text{mass of hydrogen in compound}}{\text{molar mass of the compound}} \quad (4)$$

From the calculations, MgH_2 exhibits the highest hydrogen storage capacity at 7.66 wt%, consistent with its lightweight elemental nature and strong hydrogen affinity.[53,54] This high gravimetric capacity underscores MgH_2's long-standing position as a benchmark hydrogen storage material, despite its high desorption temperature and sluggish kinetics. In contrast, pristine NbH_2 has a significantly lower hydrogen capacity of 2.124 wt%, which can be attributed to the heavier atomic weight of niobium and a lower hydrogen-to-metal ratio. However, when Mg is incrementally introduced into the NbH_2 lattice to form ternary hydrides—Mg-NbH_2 (3.326%), Mg_2-NbH_2 (2.797%), and Mg_3-NbH_2 (2.378%), a nonlinear but significant improvement in hydrogen capacity is observed relative to pure NbH_2. This increase is primarily due to the incorporation of lighter Mg atoms into the matrix, which reduces the overall molecular weight of the hydride without proportionally sacrificing the hydrogen content. Interestingly, the capacity peaks at Mg-NbH_2 and slightly declines as more Mg is added (Mg_2 and Mg_3), likely due to saturation of substitutional sites or a shift in phase stability toward less hydrogen-rich or more stable

Table 3 Calculated elastic constants (C_{11}, C_{12}, C_{44}) and derived mechanical parameters including bulk modulus (B), shear modulus (G), Young's modulus (E), and Poisson's ratio (ν) for NbH_2, MgH_2, and Mg-substituted NbH_2 compounds (Mg-NbH_2, Mg_2-NbH_2, Mg_3-NbH_2) using the GGA–PBE method. These parameters provide insight into the mechanical stability, ductility, and stiffness of the hydride materials

Elastic moduli (GPa)	NbH_2	Mg-NbH_2	Mg_2-NbH_2	Mg_3-NbH_2	MgH_2
$C_{11} > 0$	257.15	179.28	176.68	360.03	95.60
C_{12}	102.94	102.59	39.92	165.62	−26.12
$C_{44} > 0$	111.15	44.32	38.33	−8.03	−9.27
$C_{11} + 2C_{12} > 0$	463.03	384.46	256.52	691.27	43.36
$C_{11}–C_{12} > 0$	154.21	76.69	136.76	194.41	121.72
Bulk modulus (B)	156.96	126.64	78.83	68.56	23.76
Shear modulus (G)	106.45	38.74	58.38	70.53	20.19
Young modulus (E)	260.47	105.46	140.47	157.56	47.21
Pugh ratio (B/G)	1.47	3.27	1.35	0.97	1.18
Anisotropic factor (A)	0.21	0.37	0.55	−9.67	1.07
Poisson ratio (υ)	0.23	0.41	0.22	1.59	−10.14

Table 4 Structural parameters of NbH_2, MgH_2, and Mg-substituted NbH_2 compounds after hydrogen desorption, calculated using the GGA–PBE method. Reported values include unit cell volume, density, lattice constants, total energy, enthalpy, and bulk modulus. The data highlight the structural evolution and thermodynamic implications of hydrogen release

Compounds	Unit volume ($Å^3$)	Unit density (g cm^{-3})	Lattice constants			Total energy (eV)	Enthalpy (eV)	Bulk modulus (GPa)	Frequency (cm^{-1})
			a/Å	b/Å	c/Å				
NbH_2	76.12	8.28	4.91	3.60	4.36	−6625.08	−6.63	1172.09	1668
Mg-NbH_2	74.99	10.56	3.78	4.65	4.27	−6658.70	−6.66	133.54	7709.70
Mg_2-NbH_2	77.45	12.31	4.01	4.81	4.01	−6692.73	−6.69	94.60	1321.48
Mg_3-NbH_2	81.58	13.67	4.30	4.42	4.30	−6726.11	−6.73	355.18	6151.39
MgH_2	93.09	1.88	4.54	4.53	4.53	−6760.63	−6.76	385.95	1668

configurations. This suggests that while Mg improves the H/M (hydrogen-to-metal) ratio initially, excessive substitution may hinder additional hydrogen uptake.

Compared to the state-of-the-art systems, these Mg-NbH_2 variants offer moderate hydrogen capacities, bridging the gap between high-capacity but kinetically limited MgH_2, and low-capacity but stable intermetallic hydrides like $LaNi_5H_6$ (∼1.4%) or TiFe (∼1.9%).[55,56] Moreover, the bonding and electronic analysis in earlier sections indicate that Mg incorporation weakens the H–H-metal bonding strength, potentially enhancing desorption kinetics, an important advantage over pure MgH_2. In conclusion, although the gravimetric hydrogen capacities of the Mg-NbH_2 systems are lower than that of pure MgH_2, they present a promising trade-off between capacity, bonding strength, and structural stability. Their performance may be further enhanced through doping, nanostructuring, or hybridization, making them viable candidates for next-generation solid-state hydrogen storage materials.

Upon desorption of hydrogen from the compounds, as modelled using the PBE functional, several significant structural and energetic changes are observed. For all systems, there is a notable decrease in total energy and enthalpy compared to the hydrogenated structures, though the trend of increasing thermodynamic stability with increasing Mg content remains consistent. The total energies for NbH_2, Mg-NbH_2, Mg_2-NbH_2, Mg_3-NbH_2, and MgH_2 after hydrogen desorption are −6625.08 eV, −6658.70 eV, −6692.73 eV, −6726.11 eV, and −6760.63 eV, respectively, with corresponding enthalpy values ranging from −6.63 eV to −6.76 eV. These values suggest that desorption slightly lowers the enthalpic stability of each compound compared to its hydrogenated counterparts but does not significantly disrupt the stability hierarchy. Structurally, desorption leads to a reduction in unit volume for all compounds except Mg_3-NbH_2, which expands slightly. NbH_2 shows the largest contraction in unit volume from 96.65 $Å^3$ to 76.12 $Å^3$, indicative of lattice shrinkage upon hydrogen removal. The increase in unit density from 6.52 g cm^{-3} to 8.28 g cm^{-3} for NbH_2 and up to 13.67 g cm^{-3} for Mg_3-NbH_2 also supports this compaction behavior. Lattice constants adjust accordingly, with varying degrees of anisotropic distortion depending on Mg content. Notably, NbH_2 exhibits angular distortions after desorption, with $\alpha = 80.95°$, $\beta = 89.98°$, and $\gamma = 90.04°$, indicating a departure from ideal cubic symmetry and a transition toward a slightly distorted or monoclinic-like structure. All other compounds exhibit 90°.

The bulk modulus values post-desorption exhibit notable variation. For example, Mg-NbH_2 shows a dramatic drop in bulk modulus to 133.54 GPa, indicating a softer and more compressible structure, whereas NbH_2 maintains a relatively high modulus of 1172.09 GPa. These differences suggest that Mg incorporation affects the mechanical rigidity of the structure more significantly after hydrogen release. Vibrational frequency data reveal sharp contrasts as well. The frequency remains at 1668 cm^{-1} for NbH_2 and MgH_2, implying similar vibrational modes post-desorption. However, Mg-NbH_2 shows an extremely high frequency of 7709.70 cm^{-1}, suggesting the emergence of highly localized or stiff vibrational modes, potentially due to structural rearrangements or residual stress within the desorbed lattice. Overall, hydrogen desorption leads to structural compaction, modest decreases in enthalpic stability, and changes in mechanical and vibrational properties. The general trend of increasing Mg content enhancing the stability of the system is preserved, while significant modifications in lattice structure and dynamics point to complex desorption-driven behavior in these metal hydride materials (Table 4).

4. Conclusions

This study presents a comprehensive density functional theory (DFT) investigation of NbH_2, MgH_2, and Mg-substituted NbH_2 systems (Mg-NbH_2, Mg_2-NbH_2, and Mg_3-NbH_2), aimed at exploring their structural, electronic, optical, and hydrogen storage properties for multifunctional energy applications. The substitution of Mg into the fluorite-type NbH_2 matrix leads to notable structural distortions, increasing unit cell volume and density, and introducing flexibility in the lattice geometry. Among the computational approaches, GGA/PBE proved more effective than HSE03 in capturing these trends realistically, especially under varying Mg content. Electronic analysis revealed a transition from metallicity in NbH_2 and its Mg-substituted counterparts to semiconducting behavior in MgH_2, underscoring the tunability of electronic properties *via* controlled doping. The total density of states (TDOS) decreased with increasing Mg content, suggesting reduced carrier density and modified electronic transport characteristics. Optically, Mg-NbH_2 exhibited superior dielectric strength and refractive index, positioning it as the most

promising candidate for optoelectronic and plasmonic applications, while MgH_2 showed dominant reflectivity and optical conductivity in the UV-visible range.

From a mechanical standpoint, NbH_2 demonstrated high rigidity and elastic stability, whereas Mg doping progressively enhanced ductility but at the cost of mechanical stability, especially in Mg_2-NbH_2 and Mg_3-NbH_2, where instability indicators such as negative shear constants and unrealistic Poisson ratios were observed. In terms of hydrogen storage, MgH_2 retained the highest gravimetric capacity (7.66 wt%), but its known drawbacks such as slow desorption kinetics highlight the need for alternatives. The Mg-NbH_2 compounds showed moderate hydrogen capacity (2.4–3.3 wt%) and offer a promising trade-off between structural stability, storage potential, and functional versatility. In summary, this work identifies Mg-NbH_2 as a tunable material system with balanced performance across hydrogen storage, optoelectronics, and mechanical robustness. The insights gained here provide a rational design strategy for developing next-generation metal hydrides with multifunctional energy applications.

Data availability

Data will be made available upon request.

Conflicts of interest

There are no conflicts to declare.

Acknowledgements

We acknowledged the centre for High-Performance Computing Centre, South Africa for the computational resources.

References

1 F. Qureshi, M. Yusuf, H. Kamyab, D. V. N. Vo, S. Chelliapan, S. W. Joo and Y. Vasseghian, Latest eco-friendly avenues on hydrogen production towards a circular bioeconomy: Currents challenges, innovative insights, and future perspectives, *Renewable Sustainable Energy Rev.*, 2022, **168**, 112916.

2 A. Y. Esayed and D. O. Northwood, Metal hydrides: a review of group V transition metals—niobium, vanadium and tantalum, *Int. J. Hydrogen Energy*, 1992, **17**, 41–52.

3 M. R. Ghaani, Study of New Materials and Their Functionality for Hydrogen Storage and Other Energy Applications, PhD dissertation, University of Milano-Bicocca, 2014.

4 M. Babar, A. W. Anwar, M. Moin, M. A. Ahmad, U. Thumu, A. Ali and A. Qadoos, Comparative analysis of inorganic lead halide perovskites with promising (Mg^{+2})-doped for optoelectronic applications: a computational insights, *Opt. Quantum Electron.*, 2024, **56**, 732.

5 H. T. Rouf, T. Zeeshan, M. Khalil, F. Ullah, S. M. Ramay and M. Saleem, DFT and experimental study of Mg substituted strontium oxide for optoelectronic applications, *J. Phys. Chem. Solids*, 2025, **201**, 112656.

6 R. C. Ropp, *Encyclopedia of the Alkaline Earth Compounds. Encyclopedia of the Alkaline Earth Compounds*. Newnes, 2012.

7 S. Tekumalla and M. Gupta, in *Magnesium—The Wonder Element for Engineering/Biomedical Applications*, IntechOpen, 2020.

8 M. Halka and B. Nordstrom, *Alkali and Alkaline Earth Metals*, Infobase Publishing, 2010.

9 M. I. Khan, Z. Saman, A. Mujtaba, M. S. Hasan, M. Zhang and S. Ezzine, Tailoring the structural, morphological, optical, photocatalysis, and electrical characteristics of $Zn_{0.5}Mg_{0.5-x}Co_xLa_{0.1}Fe_{1.9}O_4$ ferrites across cobalt concentration from x = 0.0–0.2, *Mater. Sci. Eng., B*, 2025, **319**, 118352.

10 P. Schouwink, M. B. Ley, A. Tissot, H. Hagemann, T. R. Jensen, Ľ. Smrčok and R. Černý, Structure and properties of complex hydride perovskite materials, *Nat. Commun.*, 2014, **5**, 5706.

11 C. Tardei, F. Grigore, I. Pasuk and S. Stoleriu, The study of Mg^2/Ca^2 substitution of-tricalcium phosphate, *J. Optoelectron. Adv. Mater.*, 2006, **8**, 568–571.

12 M. D. Y. S. Beqain, Novel Substituted Hydroxyapatites, PhD Thesis, The University of Waikato, 2023.

13 G. Costentin, C. Drouet, F. Salles and S. Sarda, Structure and Surface Study of Hydroxyapatite-Based Materials: Experimental and Computational Approaches, *Design and Applications of Hydroxyapatite-Based Catalysts*, Elsevier, 2022, pp. 73–140.

14 Z. Chuanzhao, S. Guoliang, W. Jingjing, L. Cheng, J. Yuanyuan, K. Xiaoyu and H. Andreas, Prediction of Novel High-Pressure Structures of Magnesium Niobium Dihydride, *ACS Appl. Mater. Interfaces*, 2017, **9**(31), 26169–26176.

15 H. Wenzl, Ordered and Disordered Hydrogen Interstitials in Niobium, *J. Phys. Colloq.*, 1978, **277**, 221.

16 F. D'Errico, M. Tauber and M. Just, Magnesium alloys for sustainable weight-saving approach: A brief market overview, new trends, and perspectives, *Curr. Trends Magnesium (Mg) Res.*, 2022, 13–45.

17 S. J. Clark, M. D. Segall, C. J. Pickard, P. J. Hasnip, M. J. Probert, K. Refson, M. C. Payne and Z. Kristallogr, First principles methods using CASTEP, *Z. Kristallogr. Cryst. Mater.*, 2005, **220**, 567–570.

18 J. P. Perdew, K. Burke and M. Ernzerhof, Perdew, burke, and ernzerhof reply, *Phys. Rev. Lett.*, 1998, **80**, 891.

19 I. Grinberg, N. J. Ramer and A. M. Rappe, Transferable relativistic dirac-slater pseudopotentials, *Phys. Rev. B:Condens. Matter Mater. Phys.*, 2000, **62**, 2311.

20 P. Pulay and W. Meyer, An efficient reformulation of the closed-shell self-consistent electron pair theory, *J. Chem. Phys.*, 1984, **81**, 1901–1905.

21 J. D. Head and M. C. Zerner, A Broyden—Fletcher—Goldfarb—Shanno optimization procedure for molecular geometries, *Chem. Phys. Lett.*, 1985, **122**, 264–270.

22 K. Hummer, J. Harl and G. Kresse, Heyd-Scuseria-Ernzerhof hybrid functional for calculating the lattice dynamics of

semiconductors, *Phys. Rev. B: Condens. Matter Mater. Phys.*, 2009, **80**, 115205.
23 S. J. Grabowski, What is the covalency of hydrogen bonding?, *Chem. Rev.*, 2011, **111**, 2597–2625.
24 J. Contreras-García, W. Yang and E. R. Johnson, Analysis of hydrogen-bond interaction potentials from the electron density: integration of noncovalent interaction regions, *J. Phys. Chem. A*, 2011, **115**, 12983–12990.
25 A. E. Reed, R. B. Weinstock and F. Weinhold, Natural population analysis, *J. Chem. Phys.*, 1985, **83**, 735–746.
26 H. Lu, D. Dai, P. Yang and L. Li, Atomic orbitals in molecules: general electronegativity and improvement of Mulliken population analysis, *Phys. Chem. Chem. Phys.*, 2006, **8**, 340–346.
27 X. Xiaobing, Z. Weibing, Y. Weiyang, W. Na and E. Tang Biyu, Energetics and electronic properties of Mg_2 TMH_2 (TM = Sc, Ti, V, Y, Zr, Nb): an *ab initio* study, *Phys. B*, 2009, 404.
28 P. Vajeeston, P. Ravindran, A. Kjekshus and H. Fjellvåg, High hydrogen content complex hydrides: a density-functional study, *Appl. Phys. Lett.*, 2006, **8**, 071906.
29 E. T. Nibbering and T. Elsaesser, Ultrafast vibrational dynamics of hydrogen bonds in the condensed phase, *Chem. Rev.*, 2004, **104**, 1887–1914.
30 M. M. H. Bhuiya, A. Kumar and K. J. Kim, Metal hydrides in engineering systems, processes, and devices: a review of non-storage applications, *Int. J. Hydrogen Energy*, 2015, **40**, 2231–2247.
31 L. W. Wang, Calculating the density of states and optical-absorption spectra of large quantum systems by the plane-wave moments method, *Phys. Rev. B:Condens. Matter Mater. Phys.*, 1994, **49**, 10154.
32 M. S. Khan, B. Gul, G. Benabdellah, B. Ahmad, N. H. Alotaibi, S. Mohammad and H. Ahmad, Insights into optoelectronic, thermodynamic, and thermoelectric properties of novel GePtCh (Ch = S, Se, Te) semiconductors: first-principles perspective, *Phys. Scr.*, 2024, **99**, 065939.
33 L. Zhang, X. Xiao, C. Xu, J. Zheng, X. Fan, J. Shao and L. Chen, Remarkably improved hydrogen storage performance of MgH_2 catalyzed by multivalence NbH_x nanoparticles, *J. Phys. Chem. C*, 2015, **119**, 8554–8562.
34 U. Mehmood, F. A. Al-Sulaiman, B. S. Yilbas, B. Salhi, S. H. A. Ahmed and M. K. Hossain, Superhydrophobic surfaces with antireflection properties for solar applications: a critical review, *Sol. Energy Mater. Sol. Cells*, 2016, **157**, 604–623.
35 K. Sturm, Adv. Electron energy loss in simple metals and semiconductors, *Adv. Phys.*, 1982, **31**, 1–64.
36 N. R. Abdullah, H. O. Rashid, B. J. Abdullah, C. S. Tang and V. Gudmundsson, Planar buckling controlled optical conductivity of SiC monolayer from deep-UV to visible light region: a first-principles study, *Mater. Chem. Phys.*, 2023, **297**, 127395.
37 I. Khan, A. Ullah, N. Rahman, M. Husain, H. Albalawi, A. H. Alfaifi and M. Sohail, Computational Insights into Structural, Elastic, Optoelectronic, and Thermodynamic Properties of Silver-based Germanium Ternary Halide Perovskites, *Phys. B*, 2025, 417265.
38 A. K. Sarychev and V. M. Shalaev, Electromagnetic field fluctuations and optical nonlinearities in metal-dielectric composites, *Phys. Rep.*, 2000, **335**, 275–371.
39 H. Kuzmany, The dielectric function, *Solid-State Spectrosc.: An Introduction*, 1998, pp. 101–120.
40 L. Dissado, Dielectric response, *Springer Handb. Electron. Photonic Mater.*, 2017, 1.
41 S. A. Maier and H. A. Atwater, Plasmonics: Localization and guiding of electromagnetic energy in metal/dielectric structures, *J. Appl. Phys.*, 2005, **98**, 011101.
42 J. Mistrik, S. Kasap, H. E. Ruda, C. Koughia and J. Singh, Optical properties of electronic materials: fundamentals and characterization, *Springer Handb. Electron. Photonic Mater.*, 2017, 1.
43 X. Luo, *Engineering Optics 2.0: A Revolution in Optical Theories, Materials, Devices and Systems*, 2019, pp. 107–148.
44 H. Eisenberg, Equation for the refractive index of water, *J. Chem. Phys.*, 1965, **43**, 3887–3892.
45 F. A. Nelson, A. Basem, D. J. Jasim, T. E. Gber, M. T. Odey, A. F. Al Asmari and S. Islam, Chemical effect of alkaline-earth metals (Be, Mg, Ca) substitution of BFe_2XH hydride perovskites for applications as hydrogen storage materials: a DFT perspective, *Int. J. Hydrogen Energy*, 2024, **79**, 1191–1200.
46 W. Heller, Remarks on refractive index mixture rules, *J. Phys. Chem.*, 1965, **69**, 1123–1129.
47 G. D. Thayer, An improved equation for the radio refractive index of air, *Radio Sci.*, 1974, **9**, 803–807.
48 E. Schreiber, O. L. Anderson, N. Soga and J. F. Bell, Elastic Constants and Their Measurement, *J. Appl. Mech.*, 1975, **42**(3), 747–748.
49 O. N. Senkov and D. B. Miracle, Generalization of intrinsic ductile-to-brittle criteria by Pugh and Pettifor for materials with a cubic crystal structure, *Sci. Rep.*, 2021, **11**, 4531.
50 R. F. S. Hearmon, The elastic constants of anisotropic materials, *Rev. Mod. Phys.*, 1946, **18**, 409.
51 X. Xu, R. Huang, H. Li and Q. Huang, Determination of Poisson's ratio of rock material by changing axial stress and unloading lateral stress test, *Rock Mech. Rock Eng.*, 2015, **48**, 853–857.
52 M. R. Usman, Hydrogen storage methods: Review and current status, *Renewable Sustainable Energy Rev.*, 2022, **167**, 112743.
53 A. Züttel, Materials for hydrogen storage, *Mater. Today*, 2003, **6**, 24–33.
54 A. Züttel, Hydrogen storage methods, *Naturwissenschaften*, 2004, **91**, 157–172.
55 L. E. Orgaz-Baque, Contribution à l'étude des hydrures des composés intermétalliques et leurs applications dans les pompes à chaleur chimiques, Dr thesis, Université Paris, 11, 1988.
56 E. M. Dematteis, N. Berti, F. Cuevas, M. Latroche and M. Baricco, Substitutional effects in TiFe for hydrogen storage: a comprehensive review, *Mater. Adv.*, 2021, **2**, 2524–2560.